Nanoscale

ROYAL SOCIETY OF CHEMISTRY

PAPER

View Article Online
View Journal | View Issue

Cite this: *Nanoscale*, 2025, **17**, 19302

Two-dimensional $[Co(btbH)_2(dpe)_2]\cdot DMF$ metal–organic framework-derived low-cost nanocomposites for electrochemical nitrate reduction for ammonia production†

Amrutanshu Praharaj,‡[a,b] Manjunatha Kempasiddaiah,‡[a,b] Biplab Kumar Manna,[a,b] Rajib Samanta,[a,b] Ravi Kumar Trivedi,[c,d] Tushar Khairwal[a,b] and Sudip Barman *[a,b]

Excess nitrate (NO_3^-) accumulation occurs due to an imbalanced nitrogen cycle, primarily driven by artificial nitrogen fixation. In the meantime, environmental NO_3^- buildup has a substantial adverse effect on human health and the ecosystem. The electrocatalytic nitrate reduction reaction (NO_3RR), which yields value-added compounds like ammonia (NH_3), has lately attracted attention as a viable technique for addressing environmental and energy-related concerns. The NO_3RR meets the urgent need to remove NO_3^- and produce NH_3 through an alluring electrocatalytic pathway. Thus, this paper will discuss the preparation of novel 2D $[Co(btbH)_2(dpe)_2]\cdot DMF$ metal–organic frameworks, which crystallize in the triclinic crystal system belonging to the $P\bar{1}$ space group, using a solvothermal method. Among the nanocatalysts used, metallic cobalt nanoparticles supported on nitrogen-doped carbon (CoNPs/NC-600), facilely prepared through the thermal decomposition of Co-MOFs, have been shown to be highly efficient electrocatalysts for NH_3 production from the NO_3RR. The CoNPs/NC-600 nanocomposites exhibit a maximum partial current density (PCD) of −66.03 mA cm^{-2} for NH_3 production, achieving a faradaic efficiency (FE) of 72.25% at −0.5 V *vs.* RHE. Additionally, the highest yield rate of ammonia reached a notable value of 30.79 mmol h^{-2} cm^{-2}. Furthermore, density functional theory (DFT) calculations revealed that the Co[111] surface facilitates active nitrate reduction surpassing water dissociation over the Co_3O_4[311] surface. Hence, this work provides a new design strategy for developing high-performance MOF-derived electrocatalysts for the nitrate reduction reaction (NO_3RR) aimed at NH_3 production.

Received 17th June 2025,
Accepted 20th July 2025

DOI: 10.1039/d5nr02589c

rsc.li/nanoscale

1. Introduction

Fossil energy consumption has a significant role in the rapid expansion of society, resulting in the emergence of environmental issues and the energy crisis.[1] Thus, it has been decided that the global mission should be carbon neutrality.[2] Most nations are committed to lowering their use of fossil fuels by implementing environmentally friendly chemical production practices in their businesses to meet the targets outlined in the international agreement.[3] After hydrogen, nitrogen could be an alternative to fossil fuels as it is highly abundant in nature. Living things depend on nitrogen, as it is one of the components of amino acids. However, the increased use of nitrogen-containing chemicals has brought about energy problems and environmental damage.[4]

Currently, ammonia (NH_3) is one of the most widely used industrial compounds.[5] To help feed the growing global population, the production of NH_3 is now estimated to be around 175 million tonnes annually and is predicted to rise by 3–5% annually for the next few years.[6] Today, NH_3-based fertilisers

[a]*School of Chemical Sciences, National Institute of Science Education and Research (NISER), Bhubaneswar-752050, Orissa, India. E-mail: sbarman@niser.ac.in*
[b]*Homi Bhabha National Institute, Training School Complex, Anushakti Nagar, Mumbai – 400094, India*
[c]*Department of Physics, Karpagam Academy of Higher Education, Coimbatore 641021, Tamil Nadu, India*
[d]*Centre for Computational Physics, Karpagam Academy of Higher Education, Coimbatore 641021, Tamil Nadu, India*

†Electronic supplementary information (ESI) available: Instruments and analysis; table of crystal data and structure refinement parameters; table of bond lengths of $[Co(btbH)_2(dpe)_2]\cdot DMF$; table of bond angles of $[Co(btbH)_2(dpe)_2]\cdot DMF$; ATR-IR spectra of the 2D $[Co(btbH)_2(dpe)_2]\cdot DMF$ MOF; p-XRD data of Co_3O_4/NC-500, BET data of the CoNPs/NC-600 composite; fitting equivalent circuit and table of fitting data of the impedance spectra for bare CoNPs, Co_3O_4/NC-500 and CoNPs/NC-600 composites; after stability characterization; ECSA analysis; computational details. CCDC 2364117. For ESI and crystallographic data in CIF or other electronic format see DOI: https://doi.org/10.1039/d5nr02589c

‡These authors contributed equally.

account for 50% of all agricultural production worldwide, with 85% of the NH_3 produced going towards fertiliser production.[7] Therefore, ammonia will continue to play a dominant role in the agricultural sector, supported by existing distribution and transportation networks. Additionally, it is also being explored as a potential energy carrier. The main factor boosting NH_3's potential as an energy carrier is its high volumetric energy density (15.6 MJ L^{-1}), which is more than three times higher than that of Li-ion batteries (1.73 MJ L^{-1}) and compressed H_2 (5.5 MJ L^{-1} at 70 MPa).[8] It might also develop into an energy carrier in the future.[9] The storage and transportation of hydrogen is quite complex, making ammonia a promising hydrogen carrier.[10] Unlike liquid hydrogen, which requires extreme conditions, ammonia can be easily liquefied by increasing pressure.[11]

To date, we know the Haber–Bosch process as the only way for the mass production of ammonia from a reaction between N_2 and H_2 at high temperature (~500 °C) and pressure (~300 bar).[12] However, the process is energy-intensive and requires the use of fossil fuels to generate H_2, which results in high operating costs, and as a byproduct, it also emits CO_2. Currently, the world relies on the Haber–Bosch (HB) process for the production of NH_3. It emits more than 450 million metric tonnes of CO_2 (−2.9 tCO_2 per t_{NH_3}) annually and uses over 5.5 EJ of energy (38 GJ per t_{NH_3}).[13,14] The nitrogen reduction reaction (NRR), a promising ambient electrochemical pathway, has the potential to serve as an alternative to the energy-intensive Haber–Bosch process.[15–18] However, the NRR usually experiences a significantly poor NH_3 yield as well as FE due to the extremely low solubility of N_2, highly stable N≡N bond with a bond energy of 941 kJ mol^{-1} (ref. 19) at room temperature, and the intensely competitive hydrogen evolution reaction (HER), which occurs at almost the same potential.[6] Thus, an alternative approach for the selective production of ammonia is essential.

In nitrate (NO_3^-), the N=O bond has a low dissociation energy of 204 kJ mol^{-1} (ref. 20 and 21) and is highly soluble in water. As a result, NO_3^- electroreduction to NH_3 (NO_3RR) is more energetically advantageous for NH_3 production than the NRR.[22–25] In the meantime, NO_3^-, a frequent and hazardous environmental pollutant, is present in large amounts in industrial and sanitary wastewater.[26] Consequently, the NO_3RR offers a potential path toward simultaneously achieving ammonia production and environmental remediation. Instead of requiring an abundance of H_2 or other reducing agents, the NO_3RR employs electricity to reduce protons in the aqueous phase of nitrate, converting them into products like N_2, NH_3, *etc*.[27] Therefore, the NO_3RR may offer a viable substitute for the HB process while also offering a way to address the world nitrogen cycle's imbalance.[28] In the NO_3RR, electrocatalysts and their effectiveness are frequently assessed using three parameters: durability, selectivity, and catalytic activity. The cost of the electrocatalysts and the FE of the NO_3RR are also essential considerations for scale-up, as they raise the energy consumption and construction costs of electrochemical systems. Also, the NO_3RR is strongly impacted by the competitive hydrogen evolution reaction (HER). Thus, finding catalyst materials that satisfy all of these requirements is still tricky.[29]

Metal ions or clusters linked by organic ligands are known as metal–organic frameworks (MOFs). MOFs have a vast surface area and pore structure, making them functional materials for various applications, including catalysis, gas sensing, and energy storage.[30–33] Generally, MOFs can exhibit ultra-high porosity and surface areas beyond 6000 m^2 g^{-1}.[34] Porous MOFs exhibit microporous characteristics (<2 nm), but they could be typically adjusted to tune the pore diameters from several angstroms to several nanometres by varying the organic linkers.[35] At the same time, metal–organic frameworks with cobalt metal precursors have shown great promise as nitrate reduction materials because of their distinct structural characteristics and catalytic properties.[36] Because of their high electrostatic interaction with NO_3^- ions and the oxidation states (such as Co, Co^+, Co^{2+}, and Co^{3+}) Co catalysts are favourable for the adsorption and activation of NO_3^-.[14,37] Usually, cobalt ions are paired with organic ligands to create porous structures with large surface areas in these MOFs. The MOF's cobalt active sites allow effective nitrate reduction *via* electrochemical processes. The capacity of cobalt sites to adsorb nitrate molecules and aid in their conversion to nitrogen gas or ammonia is supposed to be responsible for their catalytic activity. Furthermore, the increased mass transfer of reactants and products made possible by the porous structure of cobalt-derived MOFs improves their catalytic efficacy. The worth of cobalt-derived MOFs for nitrate reduction in aqueous environments has been shown in several investigations, underscoring their potential for environmental remediation and long-term nitrate control.[38–40]

In this work, we synthesized a new 2D Co $[(btbH)_2(dpe)_2]$·DMF MOF *via* a simple solvothermal method, which was then converted into CoNPs/NC-600 composites through CVD pyrolysis. These composites outperformed bare CoNPs and Co_3O_4/NC-500 in nitrate reduction to ammonia. The CoNPs/NC-600 achieved a notable partial current density (PCD) of −66.03 mA cm^{-2} and a faradaic efficiency (FE) of 72.25% at −0.5 V (*vs.* RHE), significantly enhancing NO_3^- to NH_3 reduction while minimizing H_2 production. Also, the composite showed excellent stability over 12 hours. This improvement is attributed to higher active site exposure, better NO_3^- adsorption, and the composite's crystalline nature, electrochemical surface area, and porous structure. Furthermore, DFT calculations also revealed that Co[111] promotes hydrogenation more efficiently than Co_3O_4[311], with a lower energy barrier for $*NH_2$ to $*NH_3$ conversion. Hence, this work underscores the potential of Co-based MOF derivatives for advancing sustainable ammonia synthesis.

2. Experimental section

2.1 Chemicals required

The following chemicals were acquired from Sigma-Aldrich, Alfa Aesar, Merck, and TCI Chemicals: cobalt nitrate hexa-

hydrate [$Co(NO_3)_2 \cdot 6H_2O$], 1,3,5-tris(4-carboxyphenyl)benzene (BTB), 1,2-di(4-pyridyl)ethylene (DPE), *N*,*N*-dimethylformamide (DMF), potassium hydroxide (KOH), potassium nitrate (KNO_3), conc. sulfuric acid (H_2SO_4), and Nafion D-520 dispersion (5 wt% in isopropyl alcohol and water). Fisher Scientific provided deuterium oxide (D_2O). All chemicals and reagents, unless otherwise noted, were of analytical grade and used straight out of the container without further purification. We bought the Nafion 117 proton exchange membrane and Toray carbon cloth (TGP-H-60) from Sigma Aldrich and Alfa Aesar, respectively. Sigma Aldrich provided high-purity N_2 (99.998%) and H_2 (99.999%).

2.2 Synthesis of catalysts

2.2.1 Synthesis of the $[Co(btbH)_2(dpe)_2]$·DMF MOF. Using the solvothermal technique, a novel $[Co(btbH)_2(dpe)_2]$·DMF MOF was successfully created. Initially, solution A was created by mixing 55 mg of BTB (0.125 mmol) and 23 mg (0.125 mmol) of DPE ligands in 12.5 mL of DMF solvent. Concurrently, 37 mg (0.125 mmol) of $Co(NO_3)_2 \cdot 6H_2O$ was added to deionised H_2O to create solution B. After that, solution B was gradually added to solution A while being constantly stirred, and the resulting reaction mixture was stirred for a further 60 minutes. The resultant mixture was placed in a 50 mL stainless-steel autoclave lined with Teflon and heated to 85 °C for 72 hours. When the autoclave was allowed to cool to room temperature following the completion of the reaction, brownish red crystals of $[Co(btbH)_2(dpe)_2]$·DMF were formed. At the bottom of the autoclave, the DMF MOF appropriate for X-ray crystallography was obtained. The crystals were then dried at 60 °C after being cleaned twice with DMF and DI H_2O (2 × 10 mL). A schematic representation of the synthesis of the $[Co(btbH)_2(dpe)_2]$·DMF MOF is provided in Scheme 1.

2.2.2 Preparation of MOF-derived electrocatalysts. Initially, the as-prepared $[Co(btbH)_2(dpe)_2]$·DMF MOF was annealed under high-purity nitrogen (400 sccm) and hydrogen (50 sccm) atmospheres at 600 °C for 2 h in an tube furnace using a steady heating and cooling rate of 2 °C min^{-1}, and the resulting composite was named CoNPs/NC-600. Similarly, a Co_3O_4/NC-500 composite was also prepared by heating $[Co(btbH)_2(dpe)_2]$·DMF MOF crystals in a muffle furnace at 500 °C for 2 hours at a heating rate of 2 °C min^{-1} under an oxygen atmosphere.

2.2.3 Preparation of bare CoNPs. Bare cobalt nanoparticles (CoNPs) were prepared using the $NaBH_4$ reduction method. At first, 292 mg (1 mmol) of $Co(NO_3)_2 \cdot 6H_2O$ was dissolved in 10 mL of deionised H_2O (solution A). Simultaneously, another fresh solution containing 38 mg of $NaBH_4$ in 10 mL of deionized H_2O was prepared (solution B). After this, solution B was added dropwise to solution A and sonicated for 30 minutes. The black coloured product formed was then centrifuged, washed with deionized H_2O, and dried in an oven at 60 °C for 24 h.

2.3 Electrochemical analyses

2.3.1. Working electrode preparation. To prepare the catalyst ink, 2 mg of the prepared composite was ultrasonically sonicated for one hour in 490 μL of DI water with 10 μL of Nafion D-520 solution (5.0 wt% in isopropyl alcohol and H_2O) to form a homogeneous solution. Furthermore, to perform additional electrochemical processes, the resultant catalyst ink was then spread using a micropipette to cover a 1.0 cm^2 area on a carbon cloth and dried at 40 °C. The working electrode of the CoNPs/NC-600 composite had a metal loading of 0.67 mg cm^{-2}, quantified through an ICP-OES study.

2.3.2. Electrochemical performance. Using 1.0 M KOH as the electrolyte, an electrochemical workstation (Metrohm Autolab) equipped with an H-type undivided electrochemical cell was employed to reduce NO_3^- electrochemically. An Autolab, Metrohm, PGSTAT 320N electrochemical workstation employing a three-electrode system was used to study the electrochemical performances in this work. The working electrode was the catalyst-coated carbon cloth (1 cm^2), and the counter and reference electrodes were platinum and Ag/AgCl electrodes, respectively. The working electrode was placed in the cathodic chamber, located at 0.5 cm away from the Ag/AgCl reference electrode (saturated KCl, +197 mV *vs.* SHE). The anode and cathode chambers were separated using a "Nafion-

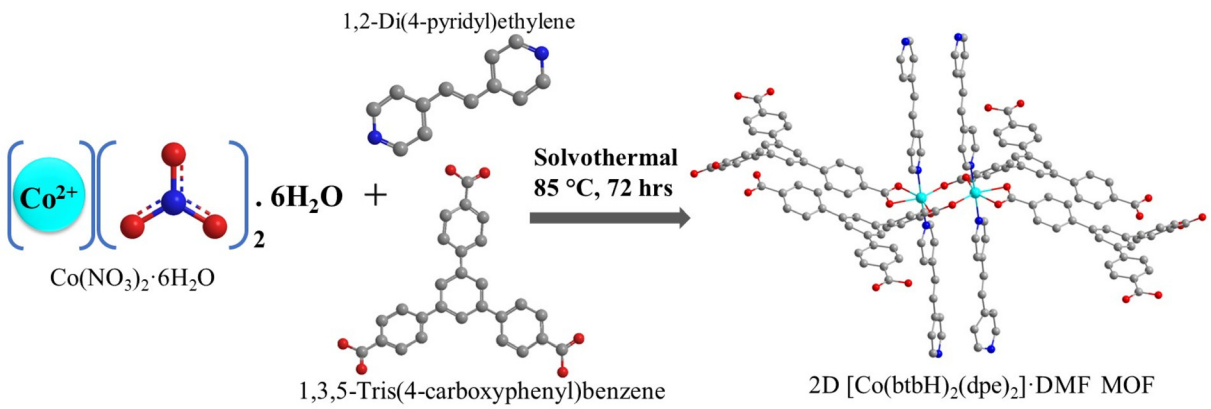

Scheme 1 Schematic illustration of syntheses of the 2D $[Co(btbH)_2(dpe)_2]$·DMF MOF.

117" membrane, each chamber having 15 mL of 1.0 M KOH electrolytic solution. Nernst's equation was used to interpret the potential measurements against Ag/AgCl to a reversible hydrogen electrode (RHE) scale (eqn (1)):

$$E_{RHE} = E_{Ag/AgCl} + 0.059 \times pH + 0.1976 \quad (1)$$

Within the potential range of +0.2 V to −0.7 V (*vs.* RHE), linear sweep voltammetry (LSV) measurements were performed at a scan rate of 30 mV s^{-1} in a solution containing 15 mL of 1.0 M KOH and 0.1 M KNO_3. Electrochemical impedance spectroscopy (EIS) was performed at −0.5 V (*vs.* RHE) with an amplitude of 10 mV over a frequency range of 1 MHz to 10 mHz. To determine the charge transfer resistance involved in the electrochemical reduction of NO_3^-, experimental data from EIS were fitted using an equivalent circuit.

2.3.3 Product analysis and quantification of NH_3. The products formed by nitrate reduction were identified and quantified by ^1H NMR spectroscopy using a water suppression method. For NMR measurements, a known concentration of formic acid (FA, Aldrich, +99.9%) was employed as an internal standard for the quantification of NH_4^+ present in the electrolyte solution. In detail, 15 mL of electrolyte after the NO_3RR was mixed with 5 mL of H_2SO_4 (4 M), to which 5 μL of formic acid (FA) was added as the internal standard. Herein, H_2SO_4 was added to the electrolyte before preparing the NMR samples to ensure an acidic solution, so that the NH_4^+ could be detected by ^1H NMR analysis. At first, NMR samples were prepared by adding 50 μL of D_2O (Aldrich, 99.9%) into 450 μL of the above electrolyte mixture, and then the ^1H NMR spectrum was recorded. The data from the recorded NMR spectra were processed using the Bruker software TopSpin (version 4.1.4). The concentration of the formed NH_4^+ in the electrolyte mixture can be determined using eqn (2):

$$m_{(NH_4^+)} = \frac{M_{(NH_4^+)} \times \frac{A_{(NH_4^+)}}{A_{(FA)}} \times m_{FA}}{n \times M_{(FA)}} \quad (2)$$

where n is the number of protons corresponding to NH_4^+ (4 protons). $m_{(NH_4^+)}$ and $m_{(FA)}$ are the concentrations of NH_4^+ and FA in the NMR test solution, respectively. $M_{(NH_4^+)}$ and $M_{(FA)}$ are the molecular weights of NH_4^+ and FA, respectively. $A_{(NH_4^+)}$ and $A_{(FA)}$ are the areas under the curves of NH_4^+ and FA, respectively. Finally, the total NH_4^+ ($m_{(NH_4^+)}$) concentration in the electrolyte can be determined based on the concentration of NH_4^+ obtained from the NMR analysis and the total volume of the electrolyte used (20 mL).

The faradaic efficiency (FE) is the ratio of electrons consumed during the NO_3^- reduction to NH_3 to the electrons consumed to produce a specific product. The following formula is used to calculate the FE for the formation of NH_3:

$$FE = \frac{N \times m_{(NH_4^+)} \times F}{I \times t} \quad (3)$$

where N and F represent the number of electrons needed to form the NH_3 product (8 electrons are required for reducing NO_3^- to NH_3) and the Faraday constant (96 485 C mol^{-1}), respectively. Here time is expressed in seconds (t) and I is the current density (j) in amperes. The total current flowing through the cathode per unit area is known as the current density (j) and is computed using the formula:

$$j = \frac{I}{A} \quad (4)$$

where A is the geometric surface area of the working electrode and I is the applied current.

The following equation was used to calculate the formation rate of NH_3 (mmol h^{-1} cm^{-2}) from the NO_3RR:

$$NH_3 = \frac{(j \times FE)}{(N \times F)} \times 3600 \quad (5)$$

where j is the current density (mA cm^{-2}).

Assuming that every Co atom on the electrode is a catalytically active site, the TOF is computed using the following equation:

$$TOF = \frac{(j \times FE)}{(N \times F \times 1000 \times n_{Co})} \quad (6)$$

where the molar quantity of Co on a 1 cm^2 × 1 cm^2 electrode is represented as n_{Co}.

3. Results and discussion

3.1. X-ray crystallography

The cobalt(II) complex, $[Co(btbH)_2(dpe)_2]$·DMF, was synthesized *via* a solvothermal process. A suitable single crystal was carefully selected and mounted for X-ray diffraction analysis. The crystallographic study revealed that the complex crystallizes in the triclinic crystal system with the space group $P\bar{1}$ (no. 2). The asymmetric unit consists of a cobalt centre coordinated by nitrogen atoms from two dpe ligands and oxygen atoms from two btb ligands. Upon examining the coordination environment, we found that the btb ligand exhibits distinct binding modes. The crystal structure elucidates the formation of a di-cobalt core, where each cobalt centre is coordinated by two nitrogen atoms from dpe ligands and two oxygen atoms from two btb ligands through a bidentate bridging mode *via* carboxylate groups. Additionally, each cobalt atom is further coordinated by another btb ligand in a bidentate chelating mode through its carboxylate functionality (Fig. 1a). The overall coordination geometry around the cobalt centre adopts a distorted octahedral arrangement. The bridging oxygen atoms (O1 and O2) form an angle of 113.62°, with a Co–O bond distance of 2.03 (6) Å, while the chelating oxygen atoms (O3 and O4) exhibit a constrained angle of 60.59° with a Co–O bond length of 2.18 (1) Å. Furthermore, the nitrogen donors are positioned in a *trans* configuration relative to the cobalt centre, with a Co–N bond distance of 2.13(4) Å (Fig. 1b). As depicted in Fig. 1c, the DMF solvent, visualized using a space-filling model, occupies the voids within the crystal lattice. Additionally, uncoordinated carboxyl groups of the btbH ligand from adja-

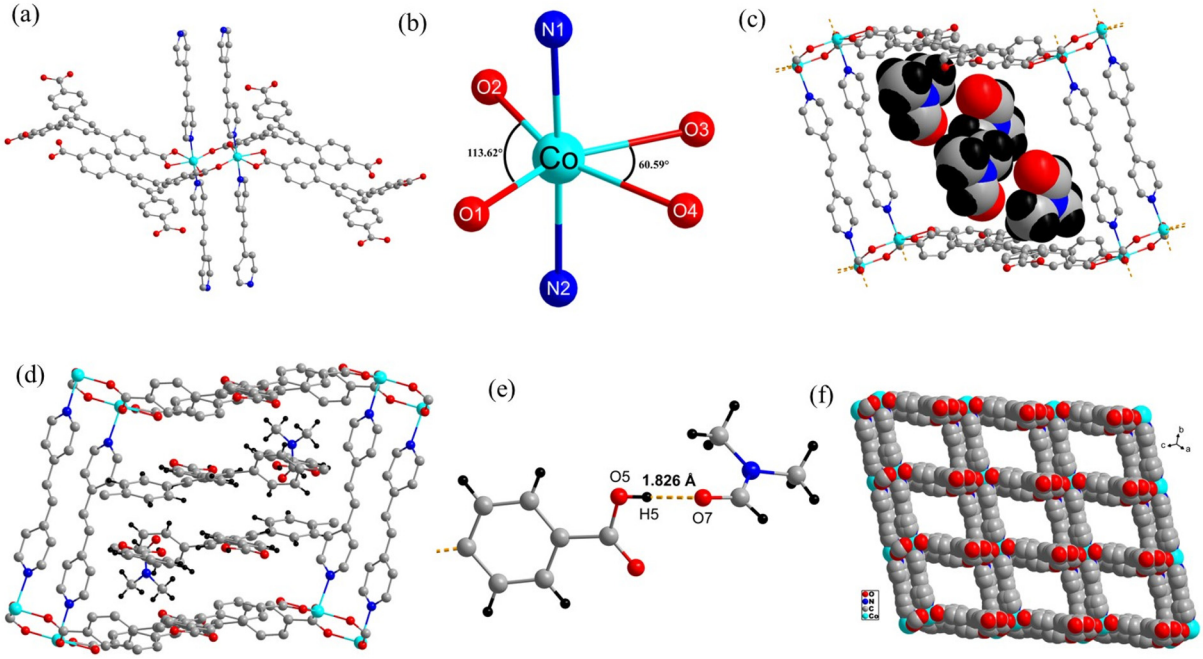

Fig. 1 The crystallographic structure of $[Co(btbH)_2(dpe)_2]\cdot DMF$, illustrating (a) ligand coordination to the di-cobalt core; (b) distorted octahedral geometry around the cobalt centre; (c) DMF solvent molecules within the crystal lattice visualized in a sphere packing mode; (d) the presence of an uncoordinated btb ligand terminal and DMF molecules within the voids; (e) hydrogen bonding interactions between the hydrogen of the uncoordinated carboxyl group and the oxygen of the DMF solvent; (f) the sphere packing diagram depicting the 2D MOF framework.

cent 2D layers reside within the voids of the metal–organic framework (MOF), aligning with the DMF solvent molecules (Fig. 1d). The DMF molecules are stabilized within the crystal structure by strong intermolecular hydrogen bonding interactions, specifically between the carboxylic hydrogen (H5) and the oxygen of the DMF molecule. The hydrogen bond parameters are O5–H5···O7 [1.826 Å, 169.38(3)°] (Fig. 1e).

The overall packing arrangement of the 2D layered structure is illustrated in Fig. 1f, where the framework exhibits a rectangular motif. Each rectangle comprises two cobalt centres positioned at the corners, linked by double-walled dpe ligands and a single btb ligand. The spatial organization and intermolecular interactions within the crystal suggest potential implications for porosity and host–guest interactions in related MOF architectures. The crystal data and structure refinement parameters and the corresponding bond lengths and bond angles of $[Co(btbH)_2(dpe)_2]\cdot DMF$ are shown in Tables S1–S3,† respectively.

3.2. Morphological and structural characterization

Analytical techniques including HR-TEM and FE-SEM were used to investigate the morphological and structural studies of the Co crystal. The TEM image of the $[Co(btbH)_2(dpe)_2]\cdot DMF$ MOF (Fig. 2a) shows aggregated micro- and nanosized crystals of the Co-MOF without any specific structural orientation; the results were in good agreement with the FE-SEM micrographs (Fig. 2b). In the course of thermal carbonization process in a tube furnace, significant changes occurred in the coordinated Co^{2+} ions within the $[Co(btbH)_2(dpe)_2]\cdot DMF$ MOF, leading to the formation of microporous CoNPs/NC-600 composites. Simultaneously, the nitrogen component present in the organic linker was successfully integrated into the carbon matrix, and both ligands were essential in the development of the nitrogen-doped carbon skeleton. First, the Co-MOF was carbonized for 2 h at a temperature of 600 °C at a heating rate of 2 °C min^{-1} under inert atmospheric conditions (a mixture of nitrogen and hydrogen gases, 400 : 50 sccm). The surface morphology of the composite following the carbonisation of the Co-MOF is shown in Fig. 2c and d. In Fig. 2c, transmission electron microscopy analysis of CoNPs/NC-600 composites reveals characteristic dark-core metallic nanoparticles (Co NPs) embedded within a nitrogen-doped carbon framework. Furthermore, the results from the field emission scanning electron microscopy (FE-SEM) images (Fig. 2d) are in agreement with these findings. HR-TEM studies were also conducted to validate the presence of Co facets in the CoNPs/NC-600 composites. Lattice fringes having an interplanar *d*-spacing of 0.199 nm are visible on the surface of CoNPs as observed in the HR-TEM image in Fig. 2e, which closely matches the crystal plane of Co(111). Additionally, the CoNPs/NC-600 composite's selected area electron diffraction (SAED) pattern is displayed in Fig. 2f. The face-centred cubic CoNPs are validated by the appearance of concentric rings in the SAED pattern, which implies that the CoNPs/NC-600 composites are nanocrystalline in nature. Furthermore, the equal distribution of Co, C, N, and O was also shown by STEM and elemental mapping analysis, confirming the existence of

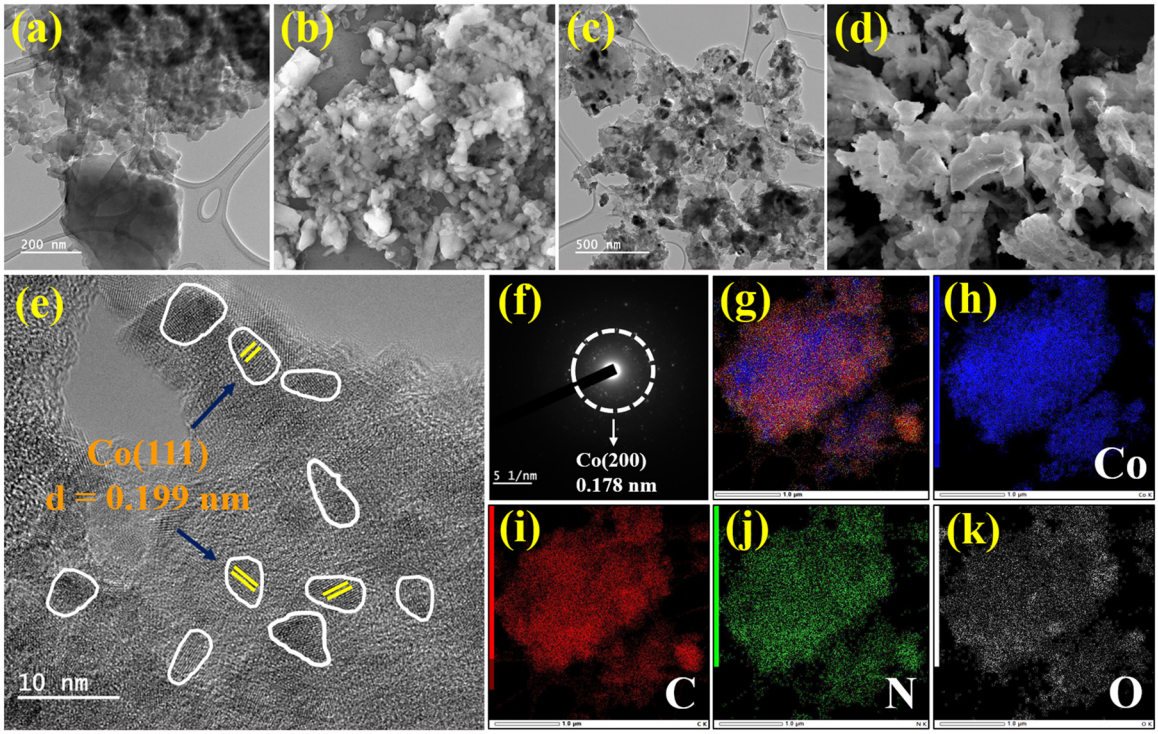

Fig. 2 (a) TEM and (b) FE-SEM images of the $[Co(btbH)_2(dpe)_2]$·DMF MOF; (c) TEM image, (d) FE-SEM image, (e) high-resolution TEM, (f) SAED pattern, and (g–k) STEM-EDS elemental mapping of CoNPs/NC-600 composites, respectively.

cobalt nanoparticle-embedded N-doped CoNPs/NC-600 composites (Fig. 2g–k).

X-ray photoelectron spectroscopy (XPS) was used to further examine the surface chemical state and composition of the $[Co(btbH)_2(dpe)_2]$·DMF MOF, as illustrated in Fig. 3a and b. The presence of Co, C, N, and O in the MOF is evident from the XPS survey scan (Fig. 3a). The Co(II) $2p_{3/2}$ and Co(II) $2p_{1/2}$ states are represented by the two distinctive peaks in the Co 2p core XPS spectrum, which are located at 780.8 eV and 796.6 eV, respectively. Further proof of the existence of divalent Co(II) ions in the Co-MOF is also provided by the emergence of shake-up satellite peaks in the binding energy range of 775 to 810 eV (Fig. 3b). Furthermore, the results of powder X-ray diffraction pattern matched the simulated XRD data and displayed a good agreement with all the diffraction peaks (Fig. 3c). Also, through the stretching and bending vibrations at 1706, 1666, 1607, 1403, 1016, 768, and 554 cm^{-1}, ATR-IR further verifies the structure of the $[Co(btbH)_2(dpe)_2]$·DMF MOF (Fig. S2†). All these results confirm that the produced $[Co(btbH)_2(dpe)_2]$·DMF MOF was highly pure and had outstanding crystallinity.

Using powder XRD patterns, the composition and crystalline nature were carefully investigated (Fig. 3d and Fig. S3a†). At first, Fig. 3d shows the p-XRD pattern of CoNPs/NC-600 composites with the distinctive peaks of Co nanoparticles (COD Number: 9008466), which agrees well with the HR-TEM results of the CoNPs/NC-600 composites. These *p*-XRD patterns demonstrate different peaks at different 2θ values of 44.3°, 51.7°, and 76°, respectively, which correspond to the crystallographic planes (−1−1−1), (−200), and (−2−20) of Co nanoparticles. Additionally, the crystal plane of Co(−1−1−1) exhibits a strong and highly powerful Braggs reflection at 2θ of 44.3°, confirming the face-centered cubic structure of Co nanoparticles. Hence, all the above HR-TEM and p-XRD data show that the porous N-doped carbon frameworks were successfully decorated with Co nanoparticles. Also, the p-XRD pattern of the Co_3O_4/NC-500 composite (COD Number: 1538531, Fig. S3a†) displays characteristic peaks corresponding to Co_3O_4, thereby confirming the formation of the Co_3O_4/NC-500 composites.

Additionally, to determine the pore size distribution, nitrogen (N_2) adsorption and desorption isotherms of the CoNPs/NC-600 composites were examined (Fig. S3b and c†). Initially, the pore size distribution study using density functional theory showed a pore radius of 1.56 nm, confirming the presence of micropores in the prepared material. The surface area of the composite was also calculated using the Brunauer–Emmett–Teller (BET) method. The CoNPs/NC-600 composite's computed specific surface area was found to be 217.7 m^2 g^{-1}. These results suggest that the composite has a porous structure that allows ions and electrolytes to pass through. By facilitating the effective transport of ions and electrolytes within the material, these pathways are essential for improving electrocatalytic kinetics and supporting the material's electrocatalytic performance.

To gain a systematic understanding of the composites's surface elemental composition, electronic characteristics, and

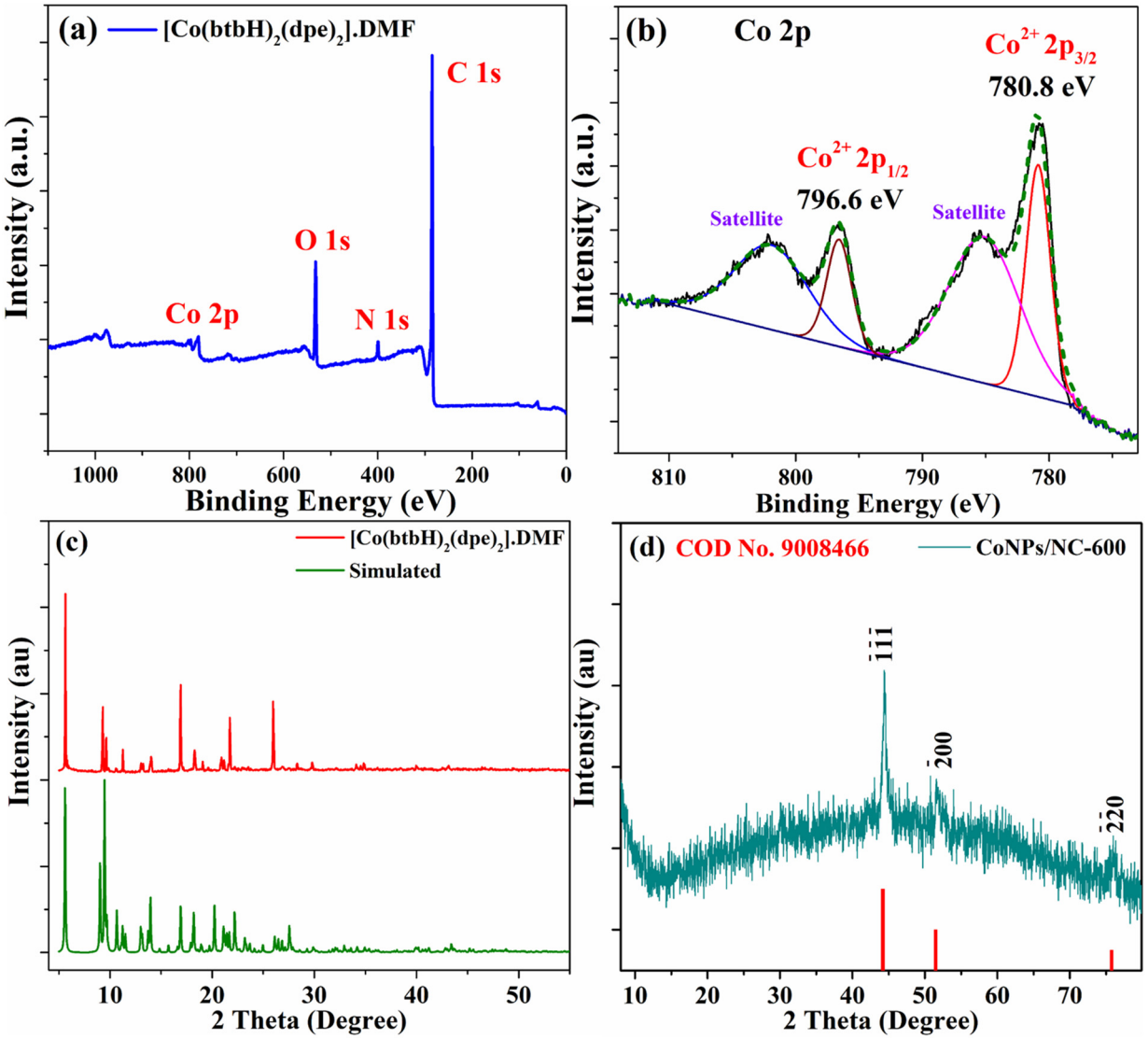

Fig. 3 Characterization of the prepared materials: (a) XPS survey spectra and (b) Co 2p high-resolution XPS spectra of the $[Co(btbH)_2(dpe)_2]$·DMF MOF; *p*-XRD patterns of the (c) $[Co(btbH)_2(dpe)_2]$·DMF MOF and (d) CoNPs/NC-600 composites.

element valence states, an additional study using X-ray photoelectron spectroscopy was carried out. Co, C, O, and N were clearly verified using the XPS survey scan of the CoNPs/NC-600 composite (Fig. 4a), which is compatible with the elemental mapping analysis results. Two prominent peaks at binding energies of 779.1 eV ($2p_{3/2}$) and 795.1 eV ($2p_{1/2}$) in the deconvoluted high-resolution XPS spectra of Co 2p were mostly associated with the metallic Co (Fig. 4b).[41] The combined results of the HR-TEM and *p*-XRD data determine that most of the composite materials were metallic Co.

However, peaks corresponding to Co(II) formation were also observed at the binding energies of 781.11 eV and 796.8 eV (Fig. 4b). Five distinct peaks were identified by further fitting the C 1s XPS spectra, as shown in Fig. 4c. These peaks were recognised as Co–C (283.7 eV), sp^2 C (284.25 eV), sp^3 C (285.1 eV), C–N/C=O (286.22 eV), and O=C–O (288.05 eV), respectively.[42] The O 1s spectrum is deconvoluted into three main components in Fig. 4d. Binding energies of 529.5, 530.22, and 531.57 eV were attributed to oxygen bonded with Co (O–Co), C=O, and C–O/C–N bonds, respectively.[43] The ICP-OES data were also obtained for CoNPs/NC-600 composites to quantify the active metal content present. From the results, it is evident that CoNPs/NC-600 composites contain 33% of Co. The higher metal content could explain the better NO_3RR activity of the CoNPs/NC-600 composite.

3.3. Electrochemical reduction of NO_3^- to NH_3

Electrocatalytic performances of the bare CoNPs, Co_3O_4/NC-500 and CoNPs/NC-600 composites towards the NO_3RR were primarily examined using the linear sweep voltammetry (LSV) method (Fig. 5). In 1 M KOH with 0.1 M KNO_3 electrolyte, the electrochemical NO_3RR was performed *versus* Ag/AgCl

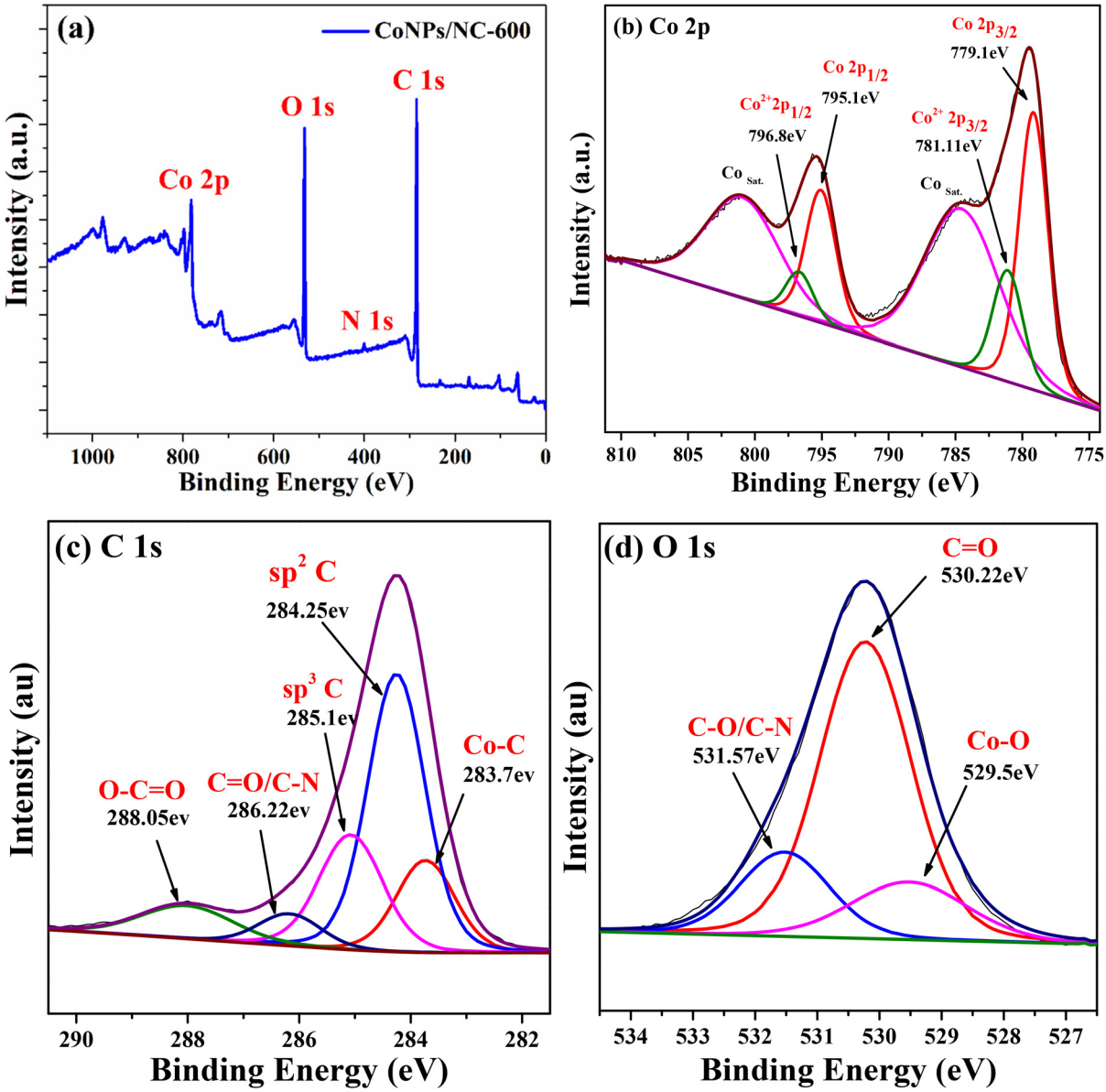

Fig. 4 X-ray photoelectron spectroscopy (a) survey scan; high-resolution (b) Co 2p, (c) C 1s, and (d) O 1s spectra of the CoNPs/NC-600 composite.

as the reference electrode. Using freshly prepared electrodes, each electrochemical experiment was recorded. The electrocatalytic performance of these composites was studied using a three-electrode electrochemical setup (undivided cell) by drop-casting the catalysts over pretreated carbon cloth (CC), which served as the working electrode substrate. Initial measurements of LSV curves were performed with NO_3^- ions being present (Fig. 5a), and the results clearly show that the as-prepared electrocatalysts can reduce the NO_3^- ions in the electrolyte. In terms of total current density across the investigated potential range *versus* RHE, Fig. 5a shows that the CoNPs/NC-600 composite performs better than the bare CoNPs and Co_3O_4/NC-500 composites. To be more precise, at −0.4 V, the CoNPs/NC-600 composite showed a current density of 52.4 mA cm^{-2}, which was significantly higher than that of the Co_3O_4/NC-500 composite (43.3 mA cm^{-2}) and bare CoNPs (6.2 mA cm^{-2}). This suggests that the CoNPs/NC-600 composite, composed of a microporous N-doped carbon skeleton, may serve as an effective electrocatalyst for NO_3^- conversion to NH_3. Further study into the electrochemical performance of CoNPs/NC-600 composites involved LSV curves with and without NO_3^- ions in the 1 M KOH electrolyte (Fig. 5b). The observed current density in the LSV curve without NO_3^- ions is most likely due to the H_2 evolution reaction (HER). The presence of NO_3^- ions in the electrolyte causes the current density to increase at a lower potential (−0.12 V, blue curve) than when the LSV is performed in 1 M KOH without NO_3^- ions (−0.41 V). This implies that the composite is active for the NO_3RR under these conditions. Similar trends were also observed for CoNPs and Co_3O_4/NC-500 composites, indicating the electro-

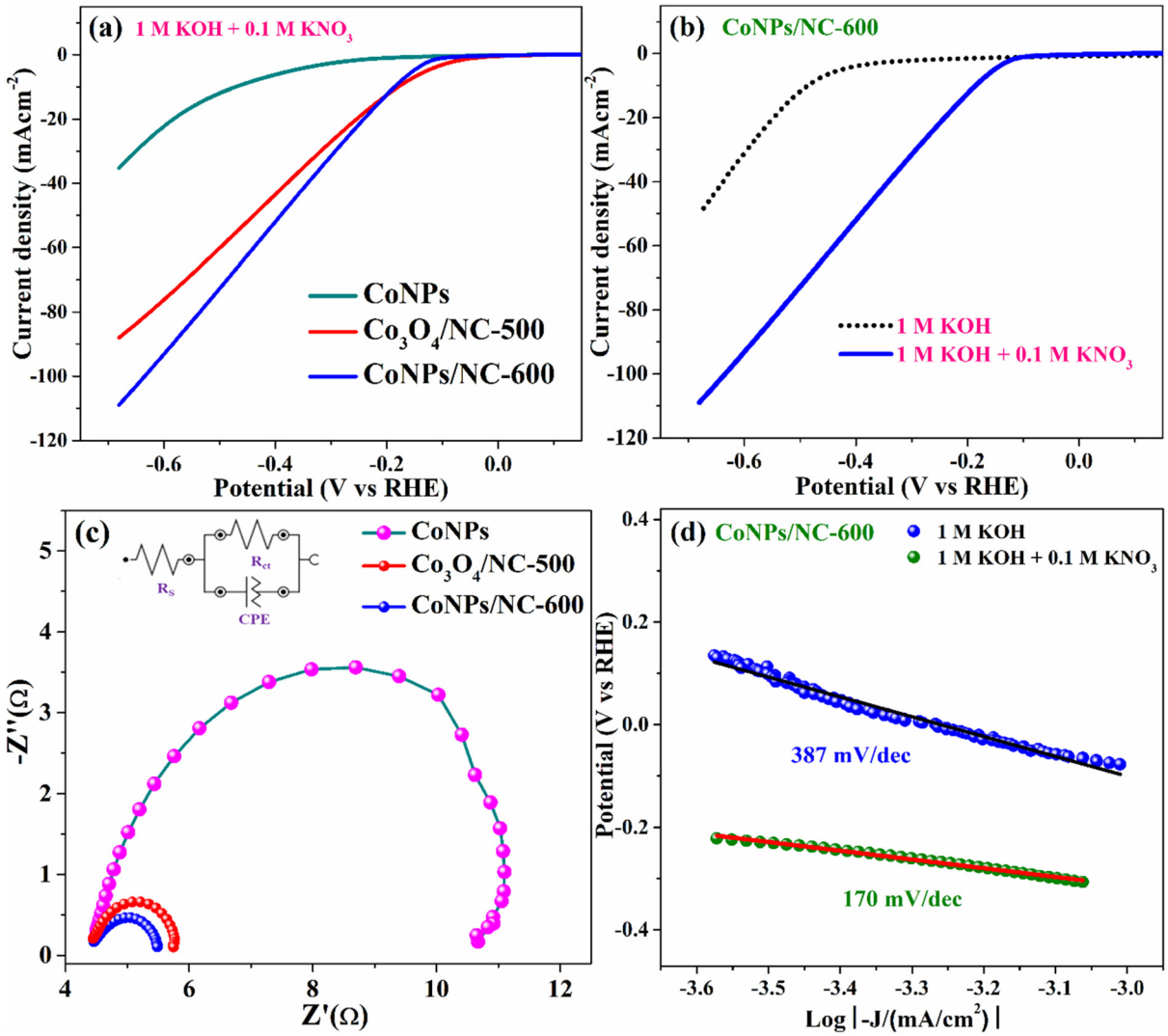

Fig. 5 (a) LSV curves in 1 M KOH with 0.1 M KNO_3 electrolyte, (b) LSV for CoNPs/NC-600 composites in 1 M KOH with and without 0.1 M KNO_3, (c) EIS plot, and (d) Tafel slopes for CoNPs/NC-600 composites in 1 M KOH with and without 0.1 M KNO_3.

chemical reduction of NO_3^- to NH_3 across these composites. This was authenticated by the dominance of NH_3 as the NO_3RR product. Furthermore, in the NO_3RR, the carbon cloth without a catalyst exhibits minimal activity, therefore its impact on current density can be omitted.

Subsequently, electrochemical impedance spectroscopy (EIS) was performed to obtain Nyquist plots for bare CoNPs, Co_3O_4/NC-500 and CoNPs/NC-600 composites (Fig. 5c). The EIS was conducted at a particular potential of −0.5 V *vs.* RHE to analyse the electron transfer process in NO_3^- ion saturated 1 M KOH aqueous electrolyte. An equivalent circuit was used in the analysis to fit the Nyquist curves of the impedance spectra (Fig. S4†), where factors such as electrolyte resistance and polarisation resistance are symbolized as R_s and R_{ct}, respectively. Table S4† shows that all composites have nearly equal ohmic resistance (R_{ohm}), with an average value of 4.45 ± 0.07 Ω due to similar electrolytes and reactor conditions. The semicircle radius is proportional to the charge transfer resistance; a smaller arc radius suggests quicker interfacial electron transport. The Nyquist plots show that the CoNPs/NC-600 composite synthesized in an inert environment had a substantial effect on the electrode's electrochemical characteristics. The arc radius of the CoNPs/NC-600 composite had the smallest R_{ct} value of 1.10 Ω, which is 5.31 and 1.2 times lower than those of CoNPs and Co_3O_4/NC-500 composites, respectively. The CoNPs/NC-600 composite demonstrates low charge-transfer resistance, implying that the composites can improve quicker charge transfer or reaction kinetics at the reaction surfaces, which is beneficial for NO_3^- reduction.

To study the kinetics of the reaction with and without the presence of NO_3^- ions, Tafel slope values were calculated using the applied potential (V *vs.* RHE) and logarithm of current density log(J (mA cm^{-2})). Fig. 5d depicts the Tafel slope of the CoNPs/NC-600 composite for both the NO_3RR and

HER processes. The Tafel slope of the CoNPs/NC-600 composite for the HER (without NO_3^- ions) is about 387 mV dec^{-1}, while it is 170 mV dec^{-1} for the NO_3^- reduction reaction. The lower slope in the case of the NO_3RR corresponds to a lower R_{ct} value and higher reaction kinetics. Thus, the CoNPs/NC-600 composite significantly promotes the production of ammonia (NH_3) over H_2 generation.

Right after observing the interesting catalytic behaviour of the bare CoNPs, Co_3O_4/NC-500 and CoNPs/NC-600 composites from the LSV curves, and to evaluate the corresponding faradaic efficiency of the NO_3RR, bulk electrolysis was performed sequentially in an H-type cell at constant potentials ranging from −0.3 to −0.6 V *vs.* RHE in 1.0 M KOH with 0.1–0.025 M KNO_3 electrolyte. Following 30 minutes of bulk electrolysis, NH_3 was detected and measured using the ^{1}H-NMR technique (see section 2.3.3 for specifics), and the results are plotted in Fig. 6 and 7.

Remarkably, NH_3 was reliably detected at a potential as low as −0.3 V *vs.* RHE, and its identification was constant and reproducible. The small deterioration of the catalytic performance at more negative potentials (>−0.6 V *vs.* RHE) could be attributed to the competing HER process. Following the chronoamperometry studies, the electrode made of CoNPs/NC-600 composites displayed a volcano-shaped curve in faradaic efficiency, peaking at −0.3 V at 63.43% (Fig. 6a). Nonetheless, CoNPs/NC-600 composites exhibit the highest faradaic efficiency for NH_3 ($FE_{ammonia}$) than bare CoNPs and Co_3O_4/NC-500 composites at nearly all studied potentials, which hinders the generation of H_2 (Fig. 6a). More specifically, the CoNPs/NC-600 composite had a higher faradaic efficiency and NH_3 production rate of 72.25% and 30.79 mmol h^{-1} cm^{-2} (0.075 M KNO_3), respectively, which were significantly greater than those of the Co_3O_4/NC-500 composite (52.5% FE) and bare CoNPs (48.75% FE) (Fig. 6b). The ^{1}H-NMR spectra of the electrolyte following the NO_3RR are shown in Fig. 6c. These spectra clearly demonstrate the generation of NH_3 through electrochemical reduction of NO_3^- ions at various applied potentials in 0.1 M KNO_3 electrolyte, with their peak intensity rising as the applied potential increases. Furthermore, many control studies were also conducted to verify the nitrogen source involved in the artificial ammonia formation. First, the amount of generated NH_3 was observed under an open circuit, *i.e.*, no current passing through the cell and in the presence of 0.1 M KNO_3 solution. This experiment shows negligible formation of ammonia after 30 minutes of electrolysis (Fig. 6d and e). Similarly, without adding NO_3^- ions to the electrolyte solution, we did not observe any visible NH_3 generation under an applied potential of −0.5 V *vs.* RHE, which was again confirmed by the ^{1}H-NMR technique (Fig. 6d and e). All things considered, our findings support the idea that NH_3 production and the level of NO_3^- ions in electrolyte are directly correlated. These findings also supported the idea that the sole nitrogen source for ammonia's electrochemical production is the presence of NO_3^- in the solution. To assess the stability of the electrocatalyst, chronoamperometry (CA) was performed under essential conditions (1.0 M KOH) for 12 hours at −0.3 V, following the addition of 1.0 M KNO_3. As shown in the graph (Fig. 6f), the initial current density was −22 mA cm^{-2}, which decreased to −19 mA cm^{-2} after 12 hours. This indicates that the prepared catalyst retains 86.6% of its initial current density even after 12 hours of electrolysis. The after-stability characterization of the material was also carried out by *ex situ* XPS, and TEM analyses. The Co 2p XPS analysis of the CoNPs/NC-600 composite confirmed the same oxidation states of Co even after electrolysis (Fig. S5a†). Moreover, the TEM image of the post-electrolysis CoNPs/NC-600 composite demonstrated that its morphology remained nearly identical to that of the fresh catalyst (Fig. S5b†). These observations are strongly supported by the HR-TEM and SAED results (Fig. S5(c and d)†), providing compelling evidence for the presence of these components.

Ultimately, the impact of the nitrate concentration on the performance was evaluated, and the electrolyte containing 0.075 M KNO_3 yielded the optimal FE for the formation of NH_3 (Fig. 7a). In this instance, we assessed the CoNPs/NC-600 composite's catalytic performance at a range of KNO_3 concentrations, which varied from 0.025 to 0.1 M. The FE for NH_3 synthesis was somewhat reduced as the NO_3^- concentration declined, which is most likely due to the increasing contribution of the competing HER. Additionally, we found that raising the KNO_3 concentration from 0.025 to 0.075 M significantly increased the NH_3 faradaic efficiency. At 0.025, 0.05, and 0.075 M concentrations of KNO_3, the maximum FEs for NO_3^- to NH_3 conversion were 69.14, 72.1, and 72.25%, respectively. It is interesting to note that as the NO_3^- concentration increased to 0.1 M, the FE of ammonia generation reduced even more. Herein, we speculate that the high concentration of NH_3 generated in this instance may not be quickly detached from the catalyst surface in a timely manner, which would cause the NO_3RR active site deactivation. In a 1.0 M KOH electrolyte containing 0.075 M KNO_3, the maximal FE of the CoNPs/NC-600 composite for the NO_3RR is 72.25%. Hence, these findings show that the CoNPs/NC-600 composite performs well in basic electrolytes in terms of the NO_3RR, which is encouraging for sustainable environmental applications (Fig. 7a). In parallel, NH_3 yield rates were computed for each NO_3RR conversion. It is evident from the plot of the NH_3 yield rate *vs.* applied potential (Fig. 7b) that a higher potential led to a higher NH_3 yield. Compared to other bare CoNPs and Co_3O_4/NC-500 composites, the product yield rate of the CoNPs/NC-600 composite was considerably higher. However, as the potential increased, the yield rate of NH_3 improved dramatically, reaching its peak performance at −0.5 V *vs.* RHE up to 30.79 mmol h^{-1} cm^{-2} (Fig. 7b). Considering the wide range of applied potentials over which the FE of NH_3 is still high, Fig. 7c shows the partial current density (PCD) of each sample. According to Fig. 7c, which shows the plot of PCD against the studied potentials, the PCD for NH_3 ($j_{ammonia}$) increased due to a rise in overpotential. Compared to other composites like bare CoNPs and Co_3O_4/NC-500 composites, the PCD of the CoNPs/NC-600 composite exhibits significantly greater $j_{ammonia}$ values. Interestingly, the $j_{ammonia}$ values of CoNPs/NC-600 (in 0.075 M KNO_3) and Co_3O_4/NC-500 (in 0.1 M KNO_3) composites

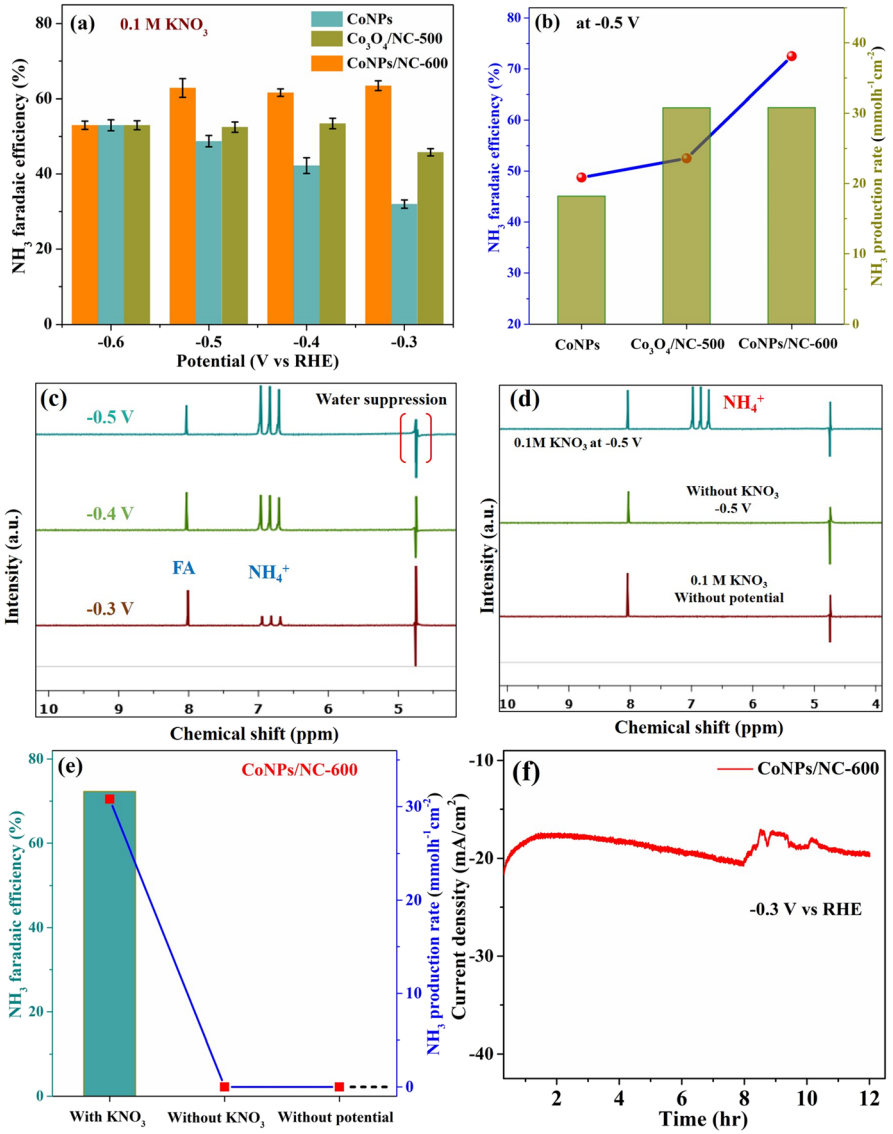

Fig. 6 (a) Potential-dependent FE for ammonia, (b) FE and the production rate of ammonia over CoNPs, Co_3O_4/NC-500 and CoNPs/NC-600 composites at −0.5 V *vs.* RHE, (c) potential-dependent ^{1}H NMR spectra; (d) ^{1}H NMR spectra and (e) FE and the production rate of ammonia over CoNPs/NC-600 composites in 1.0 M KOH electrolyte with and without NO_3^- ions at −0.5 V *vs.* RHE, and without applied potential in the presence of NO_3^- ions, respectively; (f) stability curve of the CoNPs/NC-600 catalyst at −0.3 V for 12 h.

are nearly identical when the potential is more positive than −0.5 V. However, when the potential is more negative from −0.5 V, the $j_{ammonia}$ of CoNPs/NC-600 surpasses that of the Co_3O_4/NC-500 composite. This is clearly due to the larger potential window of CoNPs/NC-600 for the high selectivity of NH_3 production. In 0.075 M KNO_3, as shown in Fig. 7c, the maximum values of the partial current density of the CoNPs/NC-600 composite for NH_3 is −66.03 mAcm^{-2} at −0.6 V.

In comparison, the $j_{ammonia}$ of bare CoNPs and Co_3O_4/NC-500 composites are −60.95 mA cm^{-2} (at −0.6 V, 0.1 M KNO_3) and −66 mA cm^{-2} (at −0.5 V, 0.1 M KNO_3), respectively. We also computed the turnover frequency (TOF) using the obtained FE, which is plotted against applied potentials in Fig. 7d. With a higher TOF value of 0.75 s^{-1} at −0.5 V *vs.* RHE, the CoNPs/NC-600 composite performs much better than other composites such as bare CoNPs and Co_3O_4/NC-500, assuming that all the Co atoms on the electrode surfaces are catalytically active.

Factors responsible for high catalytic activity:

(a) From Brunauer–Emmett–Teller (BET) analysis (Fig. S3b and c†), it is confirmed that the CoNPs/NC-600 composite has a porous structure with a high specific surface area of 217.72 m^2 g^{-1}. The electrolyte can move through it more easily because of its porous structure. This phenomenon will facilitate the transfer of mass and charge since reactants will be supplied to the cathodic surfaces rapidly, and the formed product will be released easily. Consequently, there is an increase in catalytic performance.

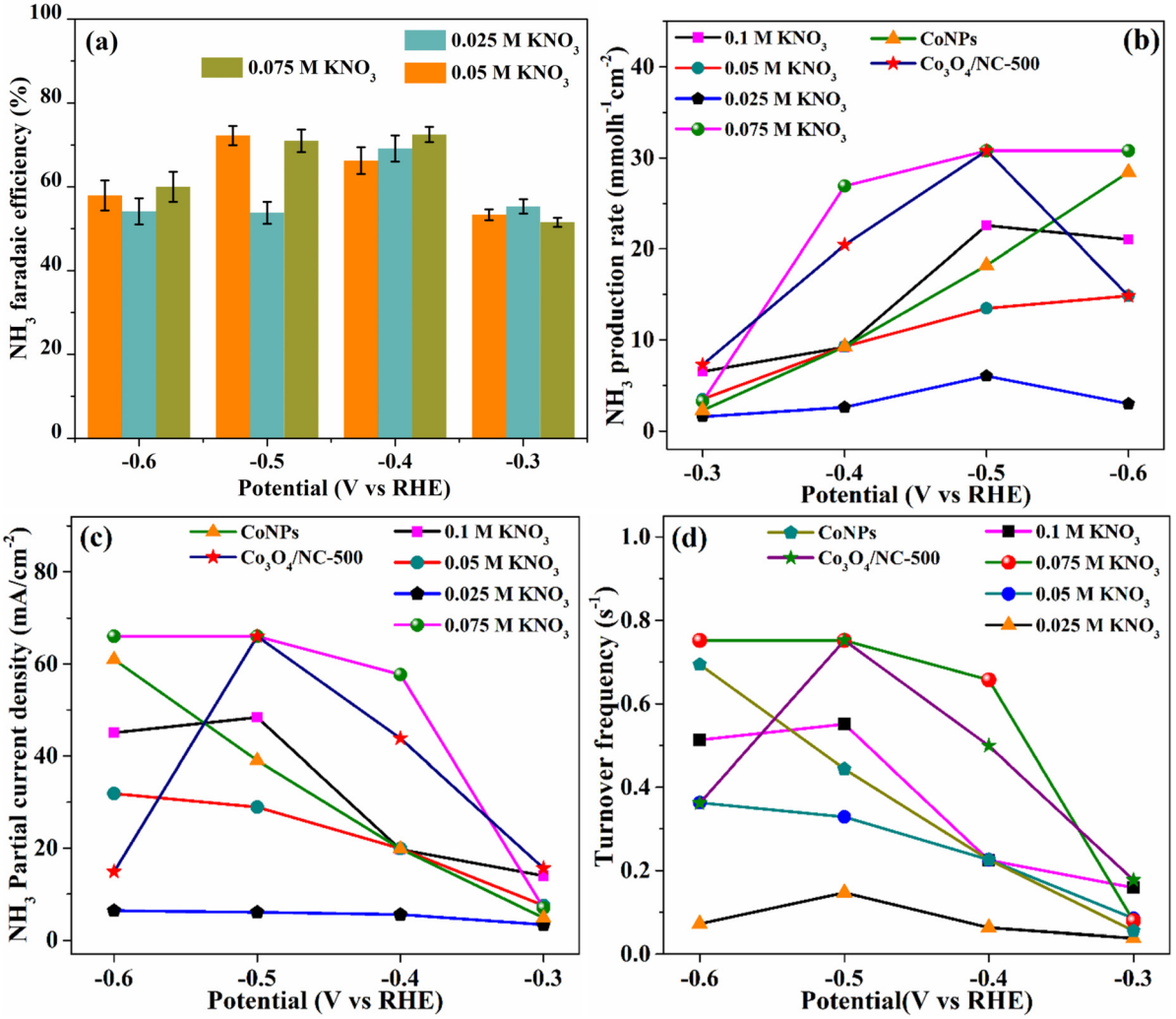

Fig. 7 Potential-dependent (a) FE for NH_3, (b) NH_3 production rates, (c) NO_3RR partial current densities, and the corresponding (d) TOF values of NH_3 over CoNPs/NC-600 composites at each studied potential from −0.3 to −0.6 V *vs.* RHE in 1.0 M KOH with different concentrations of NO_3^- (0.025 M, 0.05 M, 0.075 M and 0.1 M NO_3^- ions).

(b) The presence of a nitrogen-doped carbon framework could be another key reason for increased catalytic activity and thus the formation of NH_3. As we can see, the CoNPs/NC-600 composite exhibits better current density and faradaic efficiency than bare CoNPs. Herein, the N-doped porous carbon skeleton improves the conductivity of the CoNPs/NC-600 composite while also maintaining structural integrity, shortening ion-diffusion paths, and increasing stability.

(c) The strong catalytic activity observed may be attributed to its large electrochemically active surface area (ECSA). The catalysts' ECSA was calculated using double-layered capacitance (C_{dl}). It is commonly recognized that the catalyst's ECSA and C_{dl} are intimately correlated. Consequently, we measured the C_{dl} by cyclic voltammetry of the catalysts in 1.0 M KOH in the non-faradaic region within the 20–100 mV s^{-1} scan speed range. The plot of current density *vs.* scan rate for each composite is displayed in Fig. S6.† According to Fig. S6,† the C_{dl} values for the CoNPs/NC-600, Co_3O_4/NC-500, and bare CoNPs

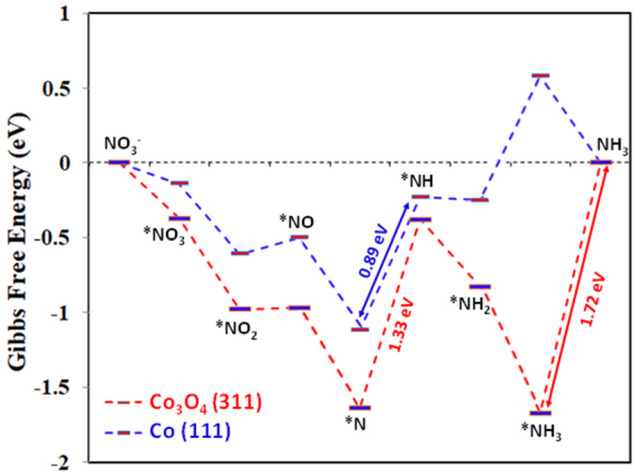

Fig. 8 Gibbs free energy for different intermediates on the Co [111] and Co_3O_4 [311] surfaces.

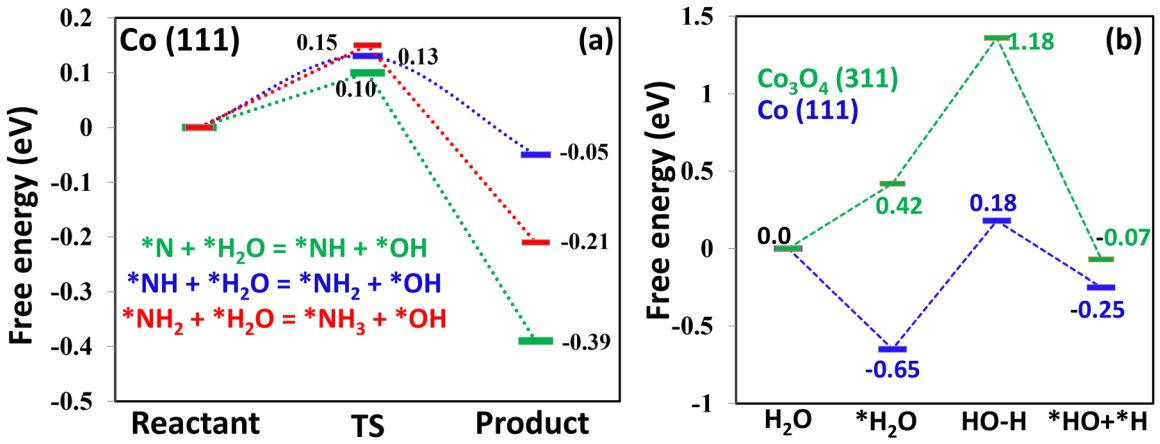

Fig. 9 (a) Reaction free energy plot for water dissociation and *N, *NH, and *NH_2 hydrogenation. (b) Reaction free energy on Co[111] and Co_3O_4[311] towards the HER (hydrogen evolution reaction).

were 0.24, 0.22, and 0.25 mF cm^{-2}, respectively. The CoNPs/NC-600 composite exhibits the highest ECSA value of 0.24 mF cm^{-2} than Co_3O_4/NC-500, implying more active sites for the electrochemical conversion of NO_3^- to NH_3 and a greater electrochemical active surface area.

These findings imply that the outstanding NO_3RR activity of the CoNPs/NC-600 composite is due to its unique structure, porous carbon nature, and higher surface area, indicating that this is a promising way to achieve an effective and highly selective NO_3RR. Also, the porous carbon skeleton improves the conductivity as well as the stability of CoNPs/NC-600 while also maintaining structural integrity.

3.4. Theoretical modelling

DFT calculations are crucial in simulating the interaction between intermediates and active substances in the electrochemical nitrate reduction process. The electrochemical reduction reaction of NO_3^- to produce NH_3 involves multiple electron and proton transfer steps.[44]

To perform DFT simulations, the Co [111] and Co_3O_4 [311] surfaces, as suggested by experimental XRD and HR-TEM investigation, are chosen as theoretical models. The NO_3RR to NH_3 on Co [111] and Co_3O_4 [311] follows multiple reaction pathways, as shown in Fig. 8. The entire optimized minimum energy configuration is displayed in ESI Fig. S7–S9.† The zero point energy and entropy correction for the Co[111] surface are shown in Table S5.†

There are generally two pathways reported in the literature.[27,45–47] The NO_3RR in the present study proceeds through NO_3^- – *NO_3 – *NO_2 – *NO – *N deoxygenation steps, followed by the *NH – *NH_2 – *NH_3 – NH_3 (g) hydrogenation steps. The rate determining step (RDS) in our present study, as shown in Fig. 8, is the conversion of *N to *NH (deoxygenation step) with a free energy (ΔG) 0.89 eV on the Co [111] surface, while the ΔG of *N to *NH for the Co_3O_4 [311] surface is 1.33 eV. For the Co_3O_4 [311] surface, the RDS is *NH_3 to NH_3 with a change in the Gibbs free energy of 1.72 eV.[48,49] It shows that the ΔG value of 0.89 eV for Co [111] in the RDS is smaller than the ΔG value of 1.72 eV for the Co_3O_4 [311] surface, which is consistent with the experimental phenomenon and thus highlights the critical role of Co in facilitating the kinetics of the NO_3^-RR. Furthermore, to get more insight into the theoretical mechanism for the change of free energy, we consider the N–H hydrogenation reaction as shown in Fig. 9a. It can be observed that the water dissociation energy barrier is around 1.18 eV, as shown in Fig. 9b, which is very high compared to the energy of 0.15 eV required for the "*NH_2 + *H_2O = *NH_3 + *OH" process. It is proposed that the hydrogenation occurs concurrently on the Co [111] surface and activates the NO_3RR process easily rather than on the Co_3O_4[311] surface.

4. Conclusions

To sum up, we successfully synthesised a new 2D Co $[(btbH)_2(dpe)_2]$·DMF MOF using a straightforward solvothermal method. Following pyrolysis in CVD, this MOF was transformed into CoNPs/NC-600 composites, which outperformed bare CoNPs and Co_3O_4/NC-500 composites in the NO_3RR to NH_3. The CoNPs/NC-600 composite achieved a partial current density of −66.03 mA cm^{-2} and a maximum faradaic efficiency of 72.25% at −0.5 V (*vs.* RHE), significantly enhancing the reduction of NO_3^- to NH_3. By significantly reducing H_2 generation, the as-prepared composite proved exceptional catalytic competences for NH_3 production while preserving the good stability over a 12 h period. This enhancement is ascribed to increased active site exposure, which raises NO_3^- adsorption levels on the catalyst surface. Additionally, the improved electrochemical performance in the NO_3RR is also a result of the composites' crystalline nature, higher electrochemical surface area, synergistic interaction within the composite, and the porous structure. Furthermore, DFT calculations also revealed that the Co[111] surface facilitates hydrogenation more efficiently than the Co_3O_4[311] surface. The hydrogenation step (*N to *NH) on Co_3O_4[311] requires a

higher Gibbs free energy (1.33 eV) than on Co[111] (0.89 eV), highlighting its superior catalytic performance. Hence, this work emphasizes the development of effective Co-based metal–organic framework derivatives to advance sustainable ammonia synthesis.

Conflicts of interest

The authors declare no competing financial interest.

Data availability

The data supporting this article have been included as part of the ESI.†

Acknowledgements

The authors are thankful to the Department of Atomic Energy (DAE) for financial support (Grant No. RIN 4002). The authors are thankful to the NISER for the infrastructure. We are also thankful to the Centre for Interdisciplinary Science (CIS), NISER, for TEM and FE-SEM facilities. We would also like to thank Subrajyoti Panda for helping in solving the crystal.

References

1 J. Wang and W. Azam, *Geosci. Front.*, 2024, **15**, 101757.
2 J. H. Williams, R. A. Jones, B. Haley, G. Kwok, J. Hargreaves, J. Farbes and M. S. Torn, *AGU Adv.*, 2021, **2**, e2020AV000284.
3 D. Liu, L. Qiao, S. Peng, H. Bai, C. Liu, W. F. Ip, K. H. Lo, H. Liu, K. W. Ng, S. Wang, X. Yang and H. Pan, *Adv. Funct. Mater.*, 2023, **33**, 2303480.
4 C. Tang and S.-Z. Qiao, *Chem. Soc. Rev.*, 2019, **48**, 3166–3180.
5 X. Luo, Y. Wu, H. Hu, T. Wei, B. Wu, J. Ding, Q. Liu, J. Luo and X. Liu, *Small*, 2024, **20**, 2403399.
6 X. Zhang, E. A. Davidson, D. L. Mauzerall, T. D. Searchinger, P. Dumas and Y. Shen, *Nature*, 2015, **528**, 51–59.
7 E. R. Morgan, J. F. Manwell and J. G. McGowan, *ACS Sustainable Chem. Eng.*, 2017, **5**, 9554–9567.
8 Y. Wang, W. Zhou, R. Jia, Y. Yu and B. Zhang, *Angew. Chem., Int. Ed.*, 2020, **59**, 5350–5354.
9 L. Zhai, S. Liu and Z. Xiang, *Ind. Chem. Mater.*, 2023, **1**, 332–342.
10 E. Spatolisano, L. A. Pellegrini, A. R. de Angelis, S. Cattaneo and E. Roccaro, *Ind. Eng. Chem. Res.*, 2023, **62**, 10813–10827.
11 D. R. MacFarlane, P. V. Cherepanov, J. Choi, B. H. Suryanto, R. Y. Hodgetts, J. M. Bakker, F. M. F. Vallana and A. N. Simonov, *Joule*, 2020, **4**, 1186–1205.
12 M. Byun, D. Lim, B. Lee, A. Kim, I.-B. Lee, B. Brigljević and H. Lim, *Appl. Energy*, 2022, **307**, 118183.
13 J. Lim, C. A. Fernández, S. W. Lee and M. C. Hatzell, *ACS Energy Lett.*, 2021, **6**, 3676–3685.
14 H. Liang, M. Chen, Y. Feng, G. Meng, J. Zhang, W. Liu and X. Liu, *Inorg. Chem.*, 2025, **64**, 1252–1257.
15 J. Deng, J. A. Iñiguez and C. Liu, *Joule*, 2018, **2**, 846–856.
16 C. Choi, G. H. Gu, J. Noh, H. S. Park and Y. Jung, *Nat. Commun.*, 2021, **12**, 4353.
17 M. Ismael and M. Wark, *Appl. Mater. Today*, 2024, **39**, 102253.
18 J. Chen, H. Cheng, L.-X. Ding and H. Wang, *Mater. Chem. Front.*, 2021, **5**, 5954–5969.
19 M. Teng, J. Ye, C. Wan, G. He and H. Chen, *Ind. Eng. Chem. Res.*, 2022, **61**, 14731–14746.
20 Y. Xiong, Y. Wang, J. Zhou, F. Liu, F. Hao and Z. Fan, *Adv. Mater.*, 2024, **36**, 2304021.
21 Y. Wang, L. Zhang, C. Wang, Z. Wang, Y. Feng and X. Liu, *Chem. Commun.*, 2025, **61**, 4399–4402.
22 H. Xu, Y. Ma, J. Chen, W.-X. Zhang and J. Yang, *Chem. Soc. Rev.*, 2022, **51**, 2710–2758.
23 J. Li, H. Li, K. Fan, J. Y. Lee, W. Xie and M. Shao, *Chem. Catal.*, 2023, **3**, 100638.
24 G. B. Truong, H. T. Duong, L. D. Vu and T. T. H. Hoang, *Eur. J. Inorg. Chem.*, 2023, **26**, e202300371.
25 Z.-Y. Wu, M. Karamad, X. Yong, Q. Huang, D. A. Cullen, P. Zhu, C. Xia, Q. Xiao, M. Shakouri and F.-Y. Chen, *Nat. Commun.*, 2021, **12**, 2870.
26 M. J. Pennino, J. E. Compton and S. G. Leibowitz, *Environ. Sci. Technol.*, 2017, **51**, 13450–13460.
27 J.-X. Liu, D. Richards, N. Singh and B. R. Goldsmith, *ACS Catal.*, 2019, **9**, 7052–7064.
28 N. Sun, Y. Guo, L. Luo, X. Cai, S. Shen and J. Zhang, *Appl. Surf. Sci.*, 2023, **624**, 157118.
29 S. Garcia-Segura, M. Lanzarini-Lopes, K. Hristovski and P. Westerhoff, *Appl. Catal., B*, 2018, **236**, 546–568.
30 P. A. Shinde, M. A. Abdelkareem, E. T. Sayed, K. Elsaid and A. G. Olabi, in *ESM*, Elsevier, 2021, pp. 414–423.
31 D. Li, A. Yadav, H. Zhou, K. Roy, P. Thanasekaran and C. Lee, *Glob. Chall.*, 2024, **8**, 2300244.
32 H. Furukawa, K. E. Cordova, M. O'Keeffe and O. M. Yaghi, *Science*, 2013, **341**, 1230444.
33 R. Freund, O. Zaremba, G. Arnauts, R. Ameloot, G. Skorupskii, M. Dincă, A. Bavykina, J. Gascon, A. Ejsmont and J. Goscianska, *Angew. Chem., Int. Ed.*, 2021, **60**, 23975–24001.
34 H. C. Zhou, J. R. Long and O. M. Yaghi, *Chem. Rev.*, 2012, **112**, 673–674.
35 H. Furukawa, K. E. Cordova, M. O'Keeffe and O. M. Yaghi, *Science*, 2013, **341**, 1230444.
36 J. Wang, C. Cai, Y. Wang, X. Yang, D. Wu, Y. Zhu, M. Li, M. Gu and M. Shao, *ACS Catal.*, 2021, **11**, 15135–15140.
37 B. Yang, Y. Zhou, Z. Huang, B. Mei, Q. Kang, G. Chen, X. Liu, Z. Jiang, M. Liu and N. J. N. E. Zhang, *Nano Energy*, 2023, **117**, 108901.
38 W. Du, Y.-L. Bai, J. Xu, H. Zhao, L. Zhang, X. Li and J. Zhang, *J. Power Sources*, 2018, **402**, 281–295.

39 N. S. Bobbitt, M. L. Mendonca, A. J. Howarth, T. Islamoglu, J. T. Hupp, O. K. Farha and R. Q. Snurr, *Chem. Soc. Rev.*, 2017, **46**, 3357–3385.
40 X. Wang and N. Ye, *Electrophoresis*, 2017, **38**, 3059–3078.
41 X. Li, Z. Ao, J. Liu, H. Sun, A. I. Rykov and J. Wang, *ACS Nano*, 2016, **10**, 11532–11540.
42 R. Samanta, R. Mishra, B. K. Manna and S. Barman, *ACS Appl. Nano Mater.*, 2022, **5**, 17022–17032.
43 J. Gomez-Bolivar, I. P. Mikheenko, R. L. Orozco, S. Sharma, D. Banerjee, M. Walker, R. A. Hand, M. L. Merroun and L. E. Macaskie, *Front. Microbiol.*, 2019, **10**, 1276.
44 H. Wan, A. Bagger and J. Rossmeisl, *Angew. Chem.*, 2021, **133**, 22137–22143.
45 J. Li, G. Zhan, J. Yang, F. Quan, C. Mao, Y. Liu, B. Wang, F. Lei, L. Li and A. W. Chan, *J. Am. Chem. Soc.*, 2020, **142**, 7036–7046.
46 Y. Wang, A. Xu, Z. Wang, L. Huang, J. Li, F. Li, J. Wicks, M. Luo, D.-H. Nam and C.-S. Tan, *J. Am. Chem. Soc.*, 2020, **142**, 5702–5708.
47 H. Niu, Z. Zhang, X. Wang, X. Wan, C. Shao and Y. Guo, *Adv. Funct. Mater.*, 2021, **31**, 2008533.
48 J. Yu, Z. Xi, J. Su, L. Li, P. Jing, X. Xu, B. Liu and J. Zhang, *ACS Mater. Lett.*, 2024, **6**, 2591–2598.
49 Z. Deng, C. Ma, Z. Li, Y. Luo, L. Zhang, S. Sun, Q. Liu, J. Du, Q. Lu and B. Zheng, *ACS Appl. Mater. Interfaces*, 2022, **14**, 46595–46602.